Ceric Ammonium Nitrate Oxidation of a Mn^{II} Complex Generates a Bis(μ-oxo)dimanganese(IV,IV) Product via a Mn^{IV}-oxo Intermediate

Yuri Lee, Anagha Puthiyadath, Shannon D. Jones, Melissa C. Denler, Patrick Murphy, Delara Mafi, and Timothy A. Jackson*

The University of Kansas, Department of Chemistry and Center for Environmentally Beneficial Catalysis, 1567 Irving Hill Road, Lawrence, KS 66045, USA.

*To whom correspondence should be addressed:
Timothy A. Jackson
Phone: (785) 864-3968
taj@ku.edu

Abstract

The oxidation of manganese complexes using ceric ammonium nitrate (CAN) are often complicated by the fact that cerium(IV) can serve as both an oxidant and a Lewis acid. In this work, we explore the reaction of CAN with the Mn^{II} complex $[Mn^{II}(OTf)(^{DMM}N4py)](OTf)$ ($^{DMM}N4py$ = *N*,*N*-bis(4-methoxy-3,5-di-methyl-2-pyridylmethyl)-*N*-bis(2-pyridyl)methylamine). We chose this complex as multiple oxidation products, including oxomanganese(IV) and bis(μ-oxo)dimanganese(III,IV) complexes, have previously been reported. We envisioned that knowledge of the spectral properties of these intermediates would aid in understanding the potential complexities of CAN oxidation reactions. The oxidation of $[Mn^{II}(OTf)(^{DMM}N4py)](OTf)$ with 2.0 equivalents CAN in 9:1 (v/v) MeCN:H_2O at 25 °C transiently forms the Mn^{IV}-oxo complex, but this species is formed in low yields and is unstable. The Mn^{IV}-oxo complex evolves to a new intermediate that had not been previously observed. At lower temperatures, the formation of this new intermediate is preceded by formation of the previously reported bis(μ-oxo)dimanganese(III,IV) complex. EPR and X-ray absorption experiments for the new intermediate provide strong evidence for its formulation as $[Mn^{IV}Mn^{IV}(\mu\text{-}O)_2(^{DMM}N4py)_2]^{4+}$. This work establishes dinuclear $Mn^{IV}Mn^{IV}$ species as products that must be considered in CAN oxidation reactions of Mn^{II} complexes and shows that both mononuclear Mn^{IV}-oxo and dinuclear $Mn^{III}Mn^{IV}$ complexes can be intermediates in such reactions.

Introduction

The Ce^{IV} ion in ceric ammonium nitrate (CAN) is a powerful oxidant ($Ce^{IV/III}$ reduction potential of +1.37 V vs. SCE in aqueous 1 M HNO_3)[1] and a strong Lewis acid.[1-4] Because of its high reduction potential, CAN is a common one-electron oxidant in organic synthesis and often serves as a sacrificial oxidant in water oxidation by transition-metal catalysts.[3, 5-10] On the basis of the high Lewis acidity of Ce^{IV} (and/ or its reduced Ce^{III} form), it has been proposed that this metal could direct a water molecule close to a transition-metal center to initiate O–O bond formation.[5] This role is similar to that of Ca^{II} in the oxygen-evolving complex (OEC) in photosystem II.[11] Due to the growing use of CAN in water oxidation, there is much interest in understanding intermediates formed when transition metals react with CAN.

Reactions of CAN with several Fe^{II} and Mn^{II} complexes have been reported to generate metal(IV)-oxo complexes, where the oxo ligand is derived from water.[12-16] Nam and co-workers reported the formation of a mononuclear Mn^{IV}-oxo complex from the reaction of $[Mn^{II}(CF_3SO_3)_2(BQCN)]$ (BQCN = *N*,*N*'-dimethyl-*N*,*N*'-bis(8-quinolyl)cyclohexanediamine; Figure 1) with 4 equiv. CAN in 9:1 MeCN:H_2O (or 9:1 acetone:H_2O) at 0 °C.[12] The proposed Mn^{IV}-oxo product showed a broad electronic absorption band at 630 nm, and electron paramagnetic resonance (EPR) experiments revealed a signal at $g_{eff} \approx 4$, which is consistent with an $S = 3/2$ Mn^{IV} center. The resonance Raman spectrum of the intermediate displayed a Mn–O vibration at 707 cm^{-1}, which is similar to values reported for Mn^{IV}-oxo species (712 to 750 cm^{-1}).[17-20] In a separate study, Sastri, Comba, and co-workers reported the formation of Mn^{IV}-oxo complexes supported by pentadentate N5 ligands in the bispidine family (L^1 and L^2 in Figure 1) by CAN oxidation.[13] Specifically, treatment of the Mn^{II} bispidine complexes with 4 equiv. CAN in 9:1 MeCN:H_2O (or 9:1 acetone:H_2O) at 5 °C resulted in the formation of the Mn^{IV}-oxo

complexes.[13] The electronic absorption spectra of these complexes showed broad near-IR bands at 970 and 975 nm, and ESI-MS data gave mass and isotope patterns consistent with $[Mn^{IV}(O)L]^{2+}$ ions (L = L^1 and L^2; see Figure 1). These procedures for forming Mn^{IV}-oxo complexes of neutral N5 ligand by CAN oxidation are notable, as many Mn^{IV}-oxo complexes supported by N5 ligands are generated by PhIO oxidation in the fluorinated solvent 2,2,2-trifluoroethanol (TFE).[21-25] Alternative routes to generate Mn^{IV}-oxo complexes that avoid the use of fluorinated solvents are desirable.

In the formation of these Mn^{IV}-oxo complexes, the Ce^{IV} is proposed to act solely as an oxidant, but reactions of certain Fe and Mn complexes with CAN have highlighted the consequences of the Lewis acidity of the Ce^{IV} and Ce^{III} ions. Fillol, Costas, Que, and co-workers reported the formation of $[(mcp)Fe^{IV}(O)(\mu\text{-}O)Ce^{IV}(NO_3)_3]^+$ (mcp = (*N*,*N*′-dimethyl-*N*,*N*′-bis(2-pyridylmethyl)-1,2-cis-diaminocyclohexane; Figure 1) from the reaction of $[Fe^{IV}(O)(mcp)]^{2+}$ and CAN in aqueous solution at 25 °C.[5] Data from cryospray ionization high-resolution mass spectrometry (CSI-HRMS) and resonance Raman experiments supported this assignment. Thus, in this reaction, the Ce^{IV} center and Fe^{IV}-oxo complex form a Lewis acid-base adduct. Similarly, Que and co-workers reported an X-ray diffraction structure of the oxo-bridged hetero-bi-metallic complex $[(N4py)Fe^{III}(O)Ce^{IV}(OH_2)(ONO_2)_4]^+$ (N4py = *N*,*N*-bis(2-pyridylmethyl)-*N*-bis(2-pyridyl)methylamine; see Figure 1).[26] This complex was generated from the reaction of $[Fe^{II}(NCMe)(N4py)]^{2+}$ and 2 equiv. CAN with 10 μL water in MeCN, or by the reaction of $[Fe^{IV}(O)(N4py)]^{2+}$ with 4.5 equiv. CAN in MeCN. The chemistry of Ce^{IV} as a Lewis acid was also highlighted in the formation of a complex with a Mn^{IV}-O-Ce^{IV} core. The $[Mn^{IV}(O)(dpaq)]^+$–Ce^{IV} species (dpaq = 2-[bis(pyridin-2-ylmethyl)]amino-*N*-quinolin-8-yl-acetamidate; see Figure 1) was generated by the reaction of $[Mn^{III}(OH)(dpaq)]^+$ and 2 equiv. CAN in 49:1 (v/v) CH_3CN:H_2O at

−40 ˚C. In a very recent example, the oxidation of $[Mn^{II}(ClO_4)(BnTPEN)]^+$ with 4 equiv. CAN results in the formation of a species with a Mn^{III}–O–Ce^{IV} core (BnTPEN = *N*-benzyl-*N*,*N*′, *N*′-tris(pyridine-2-ylmeth-yl)ethane-1,2-diamine).[27]

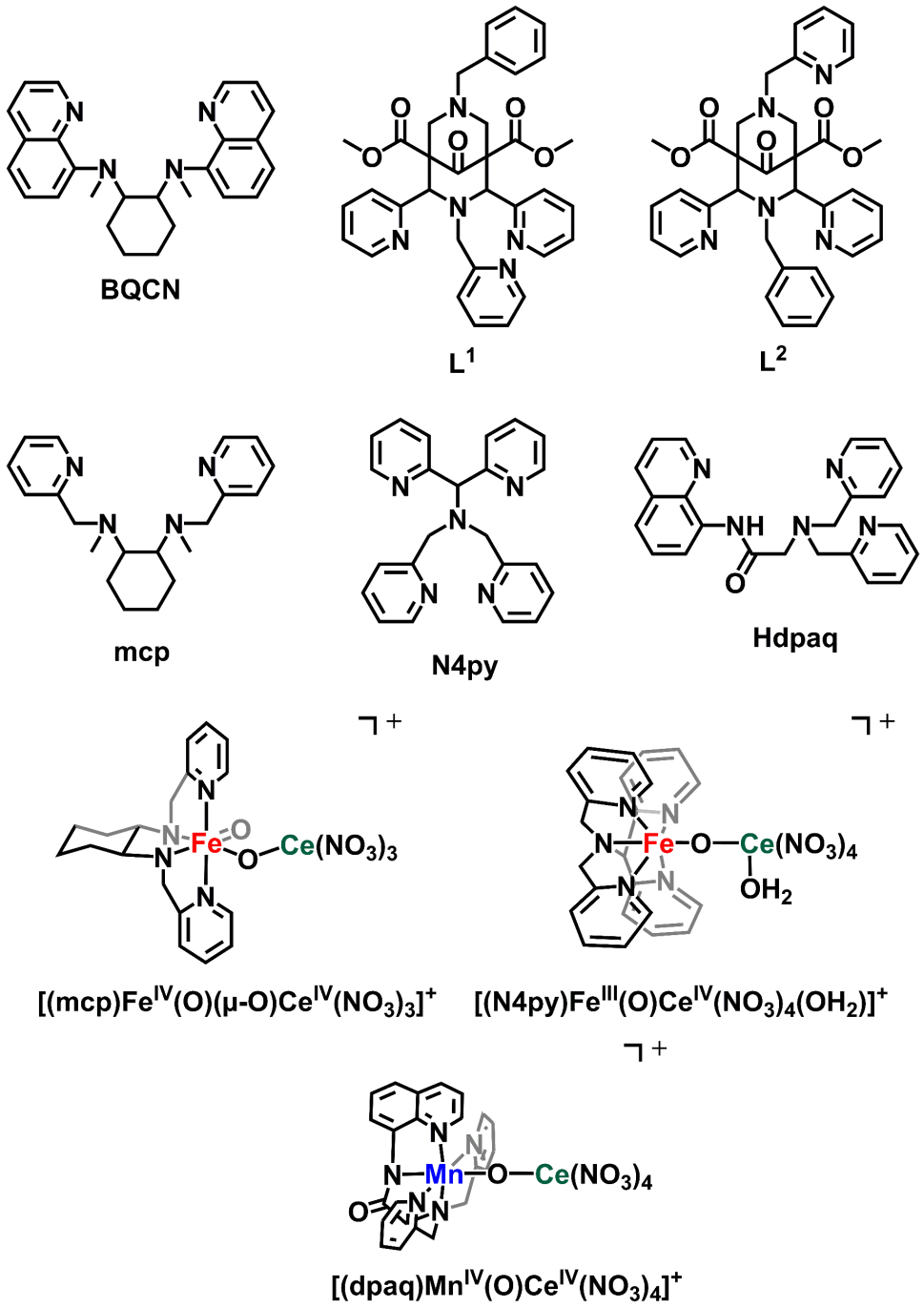

Figure 1. Ligands discussed in the text and proposed structures of Ce-bound iron or manganese species.

These studies demonstrate that the ability of the Ce^{IV} center to CAN to act as both a strong oxidant and Lewis acid can give rise to a range of products when Fe^{II} and Mn^{II} complexes react with CAN. To better understand the conditions under which CAN reacts with Mn^{II} complexes to generate Mn^{IV}-oxo species, we describe here the reactions of CAN with $[Mn^{II}(OTf)(^{DMM}N4py)](OTf)$ (**1**; see Figure 2). We chose this complex as several of its oxidation products have already been identified. For example, we have previously shown that this complex reacts with iodosobenzene (PhIO) in 2,2,2-trifluoroethanol (CF_3CH_2OH, TFE) to give the Mn^{IV}-oxo intermediate $[Mn^{IV}(O)(^{DMM}N4py)]^{2+}$ (**2**; see Figure 2).[24] Complex **2** has been characterized by electronic absorption, electron paramagnetic resonance (EPR), and Mn K-edge X-ray absorption spectroscopies and has been shown to perform C-H bond oxidation and oxygen-atom transfer reactions.[28-29] We have also demonstrated that the Mn^{II} complex **1** reacts with H_2O_2 in water to yield a complex with a bis(μ-oxo)dimanganese(III,IV) core, $[Mn^{III}Mn^{IV}(\mu\text{–}O)_2(^{DMM}N4py)_2]^{3+}$ (**3**; see Figure 2).[30] In contrast to **2**, which contains a mononuclear Mn^{IV}-oxo unit, the bis(μ-oxo)dimanganese(III,IV) unit in **3** is significantly less reactive and reacts slowly with activated O-H bonds.[30] Cyclic voltammetry experiments for **3** in CF_3CH_2OH showed a quasi-reversible process at $E_{1/2}$ = +0.74 V vs. Fc/Fc^+ (ΔE_p = 0.19 V) that was attributed to a $Mn^{IV}Mn^{IV}$ / $Mn^{III}Mn^{IV}$ couple; however the $Mn^{IV}Mn^{IV}$ species was not generated by either H_2O_2 or PhIO oxidation of **1**.[30] In this present study, we use the diagnostic electronic absorption signatures of **2** and **3** to demonstrate that these intermediates are formed when **1** is treated with CAN in a MeCN:H_2O mixture. However, under these conditions, the mononuclear Mn^{IV}-oxo complex is formed in relatively low yields and rapidly converts to a new intermediate (**4**). By combining spectroscopic data with studies of chemical reactivity, we propose that **4** is the bis(μ-oxo)dimanganese(IV,IV) complex

$[Mn^{IV}Mn^{IV}(\mu\text{–}O)_2(^{DMM}N4py)_2]^{4+}$. These studies reveal the complexity of reactions of Mn^{II} complexes with CAN.

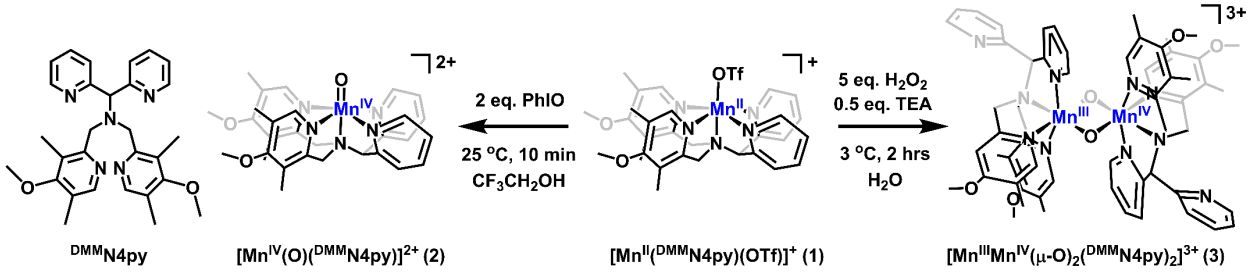

Figure 2. Structures of $^{DMM}N4py$ ligand and reported intermediates generated from $[Mn^{II}(OTf)(^{DMM}N4py)](OTf)$ under given conditions. $^{DMM}N4py$ = *N*,*N*-bis(4-methoxy-3,5-dimethyl-2-pyridylmethyl)-*N*-bis(2-pyridyl)methylamine

Experimental Methods

Materials and Instrumentation. All chemicals and solvents were ACS reagent-grade or better and purchased from commercial vendors. Chemicals were used as received unless otherwise mentioned. Electronic absorption spectra were collected using either an Agilent 8453 or a Varian Cary 50 Bio spectrophotometer, both of which were equipped with a Unisoku cryostat (USP-203-A) for temperature control. Electron paramagnetic resonance experiments were carried out using an X-band Bruker EMXPlus spectrometer (9.4 GHz) equipped with a dual-mode cavity (Bruker ER4116DM). An Oxford ITC503 cryostat controller was used to adjust the temperature along with an Oxford ESR900 continuous-flow liquid helium cryostat. X-ray absorption spectra were obtained from experiments conducted at beamline 7-3 at the Stanford Synchrotron Radiation Lightsource (SSRL) with a Si(220) monochromator and a 30-element Ge solid-state detector (Canberra) at 10 K.

Synthesis and Characterization. Synthesis and purification of $^{DMM}N4py$ were carried out according to published procedures.[24, 30-31] Formation of the $[Mn^{II}(OTf)(^{DMM}N4py)](OTf)$ complex was performed on a smaller scale than previously reported. Under an inert atmosphere, 1.2 equiv.

$Mn^{II}(OTf)_2 \cdot 2CH_3CN$[32] was dissolved in acetonitrile (0.11 g, 0.25 mmol; 15 mL) and added to ^{DMM}N4py ligand (0.1 g, 0.21 mmol), which was already dissolved in a small amount of acetonitrile (1 - 2 mL). The reaction solution was stirred overnight and filtered with a 0.45 µm PTFE syringe filter, which yielded a clear amber solution of [Mn^{II}(OTf)(^{DMM}N4py)](OTf). Recrystallization was carried out by evaporating acetonitrile from the solution of [Mn^{II}(OTf)(^{DMM}N4py)](OTf), followed by re-dissolving the residues in 1 - 2 mL acetonitrile and layering the solution with diethyl ether. Crystals were found in the solution a couple of days later or in decanted diethyl ether solution. Further purification of [Mn^{II}(OTf)(^{DMM}N4py)](OTf) was achieved using vapor diffusion from acetonitrile:diethyl ether. For independent preparations of **2** (*i.e.*, not using CAN), a solution of **1** in 2 mL 2,2,2-trifluoroethanol (CF_3CH_2OH) was reacted with 1.2 equiv. iodosylbenzene in CF_3CH_2OH and the reaction was monitored by electronic absorption spectroscopy. For independent preparations of **3** (*i.e.*, not using CAN), we treated an aqueous solution of **1** with 5 equiv. H_2O_2 (30% H_2O_2 solution in H_2O) and 0.5 equiv. triethylamine (Et_3N) at 3 °C. The reaction was stirred for 2 hours and solvent was removed under vacuum. Pure compound **3** was obtained after recrystallisation.

Electron Paramagnetic Resonance and X-ray Absorption Sample Preparation. EPR and XAS samples of **4** were generated from the reaction of **1** with 2 equiv. CAN according to the following procedures. ***Caution!*** *CAN is a strong oxidant and skin and eye irritant. This procedure controlled risk by use of millimolar concentrations of CAN.* 5 mg (0.006 mmol) **1** was dissolved in 1 mL 7:3 (v/v) MeCN:H_2O, and the solution was transferred to a quartz cuvette with a 0.2 cm pathlength. Although 9:1 (v/v) MeCN:H_2O was used for studies of 2 mM solutions of **1**, the 7:3 (v/v) MeCN:H_2O solution ensures a constant H_2O:Mn^{II} ratio for the 6 mM samples. After cooling the solution to 0 ˚C, 6.6 mg (0.012 mmol) CAN dissolved in 7:3 (v/v) MeCN:H_2O was added to

the cuvette. The reaction was monitored by electronic absorption spectroscopy. Once the absorption of the intermediate was maximized, roughly 250 μL of the solution was added to a 4 mm quartz EPR tube, or an XAS container, and flash-frozen in liquid N_2. Experimental parameters and conditions used for collecting the EPR data are provided in the appropriate figure caption. XAS data collection is discussed in the following section.

Mn *K*-edge X-ray Absorption Spectroscopy. Mn K-edge XAS data were collected at beamline 7-3 at the Stanford Synchrotron Radiation Lightsource (SSRL). XAS data were recorded using fluorescence excitation over a range of 6310 eV to 7300 eV at a temperature of 15 K. We monitored the edge position to assess any photoreduction, but photoreduction was not observed. A reference spectrum using manganese foil was simultaneously collected for the internal calibration of edge energy, of which the energy was set to 6539.0 eV. The edge energy was determined using the inflection point. XAS data were analyzed and processed using the *DEMETER* software package.[33] All data were merged at the end of processing, and the post-edge line was used for normalization. EXAFS data were fit using *FEFF6* for the phase and amplitude calculations of the models,[34] which were prepared from DFT-optimized structures (*vide infra*). The *Fityk* software was used to fit pre-edge data, using pseudo-Voigt line shapes of 1:1 Lorentzian to Gaussian functions.[35]

Electronic Structure Computations. All electronic structure computations were performed using *ORCA* 5.0.3.[36-37] The structure of $[Mn^{IV}Mn^{IV}(\mu\text{-}O)_2(^{DMM}N4py)_2]^{4+}$ was optimized using the B3LYP functional[38-39] with D3 corrections[40-41] for dispersion interactions. The calculation was converged to the $S = 0$ spin state. These calculations used def2-TZVP (Mn, N, and O) and def2-SVP (C and H) basis sets,[42-43] and the RIJCOSX approximation was used to speed the calculations. The calculations also included an SMD solvent model[44] for acetonitrile. Electronic transition

energies for **4** were determined using the TD-DFT method with the B3LYP functional [45] and the def2-TZVP basis set for Mn, O, and N atoms and def2-SVP for C and H. TD-DFT computations incorporated solvation effects from acetonitrile using the CPCM SMD solvation model.[46] The optimized coordinates for $[Mn^{IV}Mn^{IV}(\mu\text{-}O)_2(^{DMM}N4py)_2]^{4+}$ and the TD-DFT-computed electronic absorption spectrum are included in the Supporting Information

Kinetic Experiments for the Reactions of 4 and 3 with 2,4-di-tert-butylphenol. 1 mM solutions of complexes **3** and **4** were generated in 9:1 (v:v) MeCN:H_2O at 25 °C by oxidation of **1** using 1.5 and 2.0 equiv. CAN, respectively. To these solutions were added 100 μL of MeCN that delivered 40 equiv. phenol. The reactions were monitored at 25 °C by electronic absorption spectroscopy.

Results and Analysis

Reaction of $[Mn^{II}(OTf)(^{DMM}N4py)](OTf)$ with 2 equiv. CAN. Because the oxidation of the Mn^{II} complex **1** to form the mononuclear Mn^{IV}-oxo complex requires two electrons, we investigated the reaction of **1** with 2 equiv. CAN. The addition of 2.0 equiv. CAN to **1** at 25 °C in 9:1 (v/v) MeCN:H_2O leads to the immediate formation of electronic absorption bands at 640 and 960 nm (Figure 3, dashed trace). The band at 960 nm exhibits maximum intensity 14 seconds after the addition of CAN and then rapidly decays (Figure 3, inset). In contrast, the band at 640 nm maximizes in intensity 10 minutes after the addition of CAN. This species, which we refer to as **4**, has a half-life of 390 minutes at 25 °C (Figure S1). The different kinetic behavior of these electronic absorption bands allows us to associate them with distinct intermediates. The low energy band at 960 nm is assigned to the mononuclear Mn^{IV}-oxo complex **2**, as this complex displays a similar λ_{max} at 920 nm in TFE (Table 1).[24] A 15% conversion of **1** to **2** is estimated using the

extinction coefficient for **2** in TFE (ε = 290 $M^{-1}cm^{-1}$ at 920 nm in TFE).[24] The formation of **4** is insensitive to a decrease in the water content, as we observe the same reaction when **1** is oxidized with 2.0 equiv. CAN in 19:1 (v/v) MeCN:H_2O at 25 °C (Figure S2). Further, the new intermediate **4** can also be generated by treating the previously reported bis(μ-oxo)dimanganese(III,IV) complex **3** with 0.5 equiv. CAN (relative to the starting concentration of **1**; see Figure S3). The electronic absorption spectrum of the final species **4**, does not resemble spectra for known oxidation products of **1** (Table 1).[24, 30]

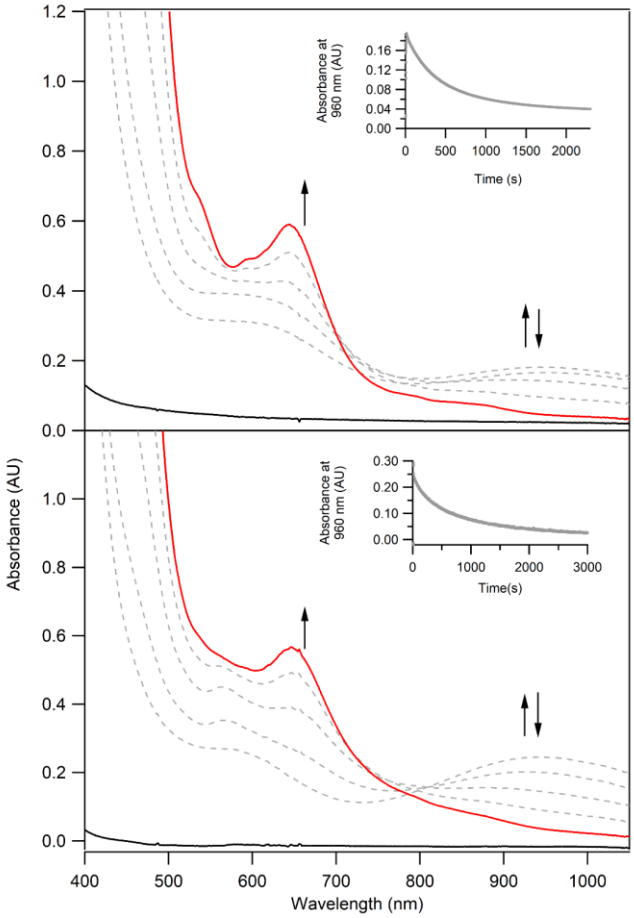

Figure 3. Electronic absorption spectra of the reaction of 2 mM [Mn^{II}(OTf)(^{DMM}N4py)](OTf) (black) and 2.0 equiv. CAN in 9:1 (v/v) MeCN:H_2O at 25 °C (top) and 0 °C (bottom). The dashed gray traces show the formation of [Mn^{IV}(O)(^{DMM}N4py)]$^{2+}$ (**2**), characterized by the band at 920 nm. As **2** evolves, we observe the formation of **4**, with bands at 535, 590, and 640 nm. The initial complex **1** has not optical bands in this spectral region.

Table 1. Electronic and X-ray Absorption Properties of $[Mn^{IV}(O)(^{DMM}N4py)_2]^{2+}$ (**2**), $[Mn^{IV}Mn^{III}(\mu\text{-}O)_2(^{DMM}N4py)_2]^{3+}$ (**3**), $[Mn^{IV}Mn^{IV}(\mu\text{-}O)_2(^{DMM}N4py)_2]^{4+}$ (**4**).[a]

	$[Mn^{IV}(O)(N4py)]^{2+}$ (**2**)[b]	$[Mn^{IV}Mn^{III}(\mu\text{-}O)_2(^{DMM}N4py)_2]^{3+}$ (**3**)[c]	$[Mn^{IV}Mn^{IV}(\mu\text{-}O)_2(^{DMM}N4py)_2]^{4+}$ (**4**)
λ (nm)	920, 580	670, 560, 440	640, 590, 535
ε ($M^{-1}cm^{-1}$)	290, 90	550, 600, 1380	585, 490, 680[d]
pre-edge (eV)	6539.9, 6541.6, 6543.2	6540.3, 6541.5	6540.5, 6541.6, 6542.9
pre-edge area	20.1	19.6	19.0
edge (eV)	6550.5	6550.6	6551.2

[a] Data for **2** and **3** in TFE. Data for **4** in 9:1 (v/v) MeCN:H_2O. [b] From ref. 24 and 28. [c] From ref. 30. [d] Extinction coefficients were determined by assuming that 100% of **1** is converted to $[Mn^{IV}Mn^{IV}(\mu\text{-}O)_2(^{DMM}N4py)_2]^{4+}$.

To better understand the reaction of **1** with 2.0 equiv. CAN, we explored this reaction at low temperatures. At 0 °C, we observe the initial formation of electronic absorption bands at 580 and 960 nm. The latter band is attributed to **2** (Table 1),[24] which is formed in higher conversion (40%) at this lower temperature. In TFE, complex **2** also displays an electronic absorption band at 580 nm, although this band has low intensity (Table 1) and cannot account for the observed intensity in the reaction of **1** with CAN. Even at 0 °C, **2** is unstable and the band at 960 nm decays over the course of ~2500 seconds (Figure 3, inset). The band at 580 nm shows a more complex evolution. Initially, this band is replaced by a set of two more intense bands at 560 and 660 nm. These bands mark the formation of the bis(μ-oxo)dimanganese(III,IV) complex **3** (564 and 667 nm absorption maxima in TFE; see Table 1).[30] These bands are transient and eventually convert to give a single prominent band at 640 nm, thus yielding the same final product (**4**) observed at 25 °C. We note that there are subtle differences between the final spectrum of **4** at 25 °C and at 0 °C, which we attribute to the incomplete conversion of **3** to **4** at 0 °C. In summary, the low-temperature reaction of **1** with 2.0 equiv. CAN generates **2** in higher yield and reveals that **3** is an intermediate on route to the product **4**. The observation that a dimanganese complex is an intermediate in the generation of **4** suggests that **4** might be a dimanganese complex that is further oxidized compared to **3**.

Reaction of [Mn^{II}(OTf)(^{DMM}N4py)](OTf) with 1.5 equiv. CAN. To test our hypothesis regarding the formulation of **4**, we first sought to generate **3** in higher yields by CAN oxidation of **1**. Upon the addition of 1.5 equiv. CAN to a 2 mM solution of **1** in 9:1 (v/v) MeCN:H_2O at 25 °C, we observed an immediate growth of two electronic absorption bands at 600 and 960 nm (Figure 4). This initial spectrum is nearly identical to that observed when 2.0 equiv. CAN are added to **1**. The near-IR band at 960 nm marks a 30% conversion of **1** to give **2**.[24] Roughly 10 seconds following its maximal formation, the broad band of **1** at 960 nm begins to decay, and the band at 600 nm evolves to give the characteristic electronic absorption features of **3** at 440, 562, and 660 nm (Figure 4). This conversion takes approximately 10 minutes. Complex **3** is indefinitely stable under these conditions and does not evolve to **4**. The known extinction coefficients for this complex (ε = 600 $M^{-1}cm^{-1}$ at 564 nm in TFE) allow us to determine a ~75% formation of the bis(μ-oxo)dimanganese(III,IV) complex from this reaction.

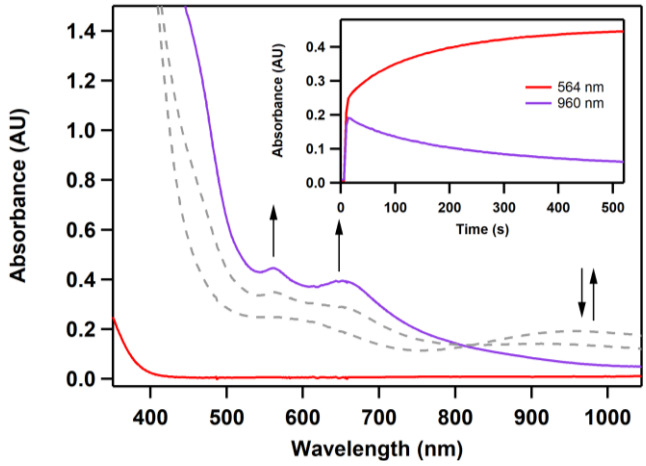

Figure 4. Electronic absorption spectra showing the reaction of 2 mM [Mn^{II}(OTf)(^{DMM}N4py)](OTf) (black) with 1.5 equiv. CAN in 9:1 (v/v) MeCN:H_2O at room temperature. The dashed gray trace shows formation of an initial intermediate, characterized by a band at 920 nm, which is converted to the product (red trace), which has bands at 440, 560, and 670 nm. The inset shows changes in absorbance at 564 and 960 nm during the initial stages of the reaction.

Chemical Conversion of 3 and 4. Our ability to generate **3** in 9:1 (v/v) MeCN:H_2O by CAN oxidation allowed us to test our hypothesis that **4** is an oxidized form of **3**. In this experiment, we first generated **3** by adding 1.5 equivalents of CAN to a solution of **1** in 9:1 (v/v) MeCN:H_2O. We then added 0.5 equiv. CAN (relative to that starting mononuclear Mn^{II} complex **1**) and observed the formation of the 640 nm band characteristic of **4** (Figure 5). The observation that **4** can also be formed upon oxidation of the $Mn^{III}Mn^{IV}$ complex **3** is consistent with the formulation of **4** as $[Mn^{IV}Mn^{IV}(\mu\text{–}O)_2(^{DMM}N4py)_2]^{4+}$. If so, addition of a one electron reductant would be able to convert this species back to **3**. To verify this proposal, 0.5 equiv. 1,1′-dibromoferrocene were added to **4**. Addition of this reductant yielded **3** in essentially quantitative yields (Figure 5). This reduced product can be converted back to **4** upon the addition of 0.5 equivalents of CAN.

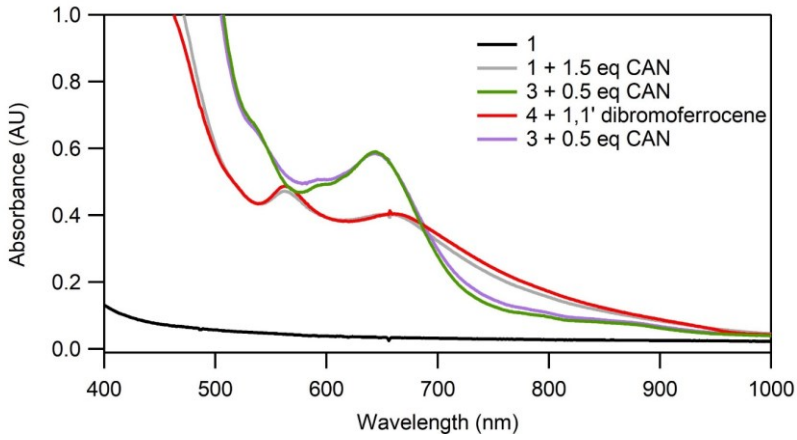

Figure 5. Electronic absorption spectra of a 2 mM solution of $[Mn^{II}(OTf)(^{DMM}N4py)](OTf)$ (**1**) before (black trace) and after (gray trace) the addition of 1.5 equiv. CAN to give **3**, which has bands at 440, 560, and 670 nm. The reaction of **3** with 0.5 equiv. CAN gives **4** (green trace), which has bands at 535, 590, and 640 nm. **4** can be reduced by the addition of 0.5 equiv. 1,1′dibromoferrocene to regenerate **3** (red trace), which can be reoxidized to **4** using 0.5 equiv. CAN (violet trace).

Collectively, our experiments provide strong support that **4** is a one-electron oxidized version of **3**. At low temperatures, **3** is observed as an intermediate that precedes the formation of **4** (Figure 3). In addition, we observe the formation of the Mn^{IV}-oxo complex **2** as an intermediate formed en

route to both **3** and **4** (Figures 3 and 4). On the basis of these observations, we have formulated the reaction scheme in Figure 7. We propose that the starting $[Mn^{II}(OTf)(^{DMM}N4py)]^{+}$ complex is initially oxidized by 1 equiv. CAN to generate an unobserved Mn^{III} species. Given the presence of water in the reaction mixture, we suggest that this species is a Mn^{III}-hydroxo complex. Attempts to generate this species by reacting **1** with 1.0 equiv. CAN were not successful, as these reactions yielded a poorly defined electronic absorption spectra, potentially implying limited stability of the Mn^{III} product (Figure S4). We propose that in the presence of an excess of CAN, a fraction (<50%) of the putative Mn^{III}-OH complex is converted to the Mn^{IV}-oxo complex **2**, consuming < 0.5 equiv. CAN. Partial oxidation is supported by the lower yields of **2** observed by optical spectroscopy (~30% yield). The reaction of **2** and the Mn^{III}-hydroxo complex generates the $Mn^{III}Mn^{IV}$ species **3**, which accumulates at lower temperatures, thereby permitting its detection by optical spectroscopy (Figure 3). When $[Mn^{II}(OTf)(^{DMM}N4py)]^{+}$ is oxidized with only 1.5 equiv. CAN, the reaction ends with **3** as the final product (Figure 4). For experiments with 2.0 equiv., **3** is further oxidized to give **4** (Figure 3), as observed in independent experiments starting with **3** and 0.5 equiv. CAN (Figure 5). An alternative mechanism would involve the reaction of **2** with **1** to give a (μ-oxo)dimanganese(III,III) complex. However, the addition of **1** to an independently prepared solution of **2** in CF_3CH_2OH (a solvent required for forming **2** in high yields) failed to show any reaction (Figure S5). Thus, at least in CF_3CH_2OH, the Mn^{IV}-oxo complex is unreactive towards **1**. In the next sections, we discuss spectroscopic data further supporting the formulation of **4** as the $[Mn^{IV}Mn^{IV}(\mu\text{–}O)_2(^{DMM}N4py)_2]^{4+}$ complex, and we explore the abilities of **4** as an oxidant.

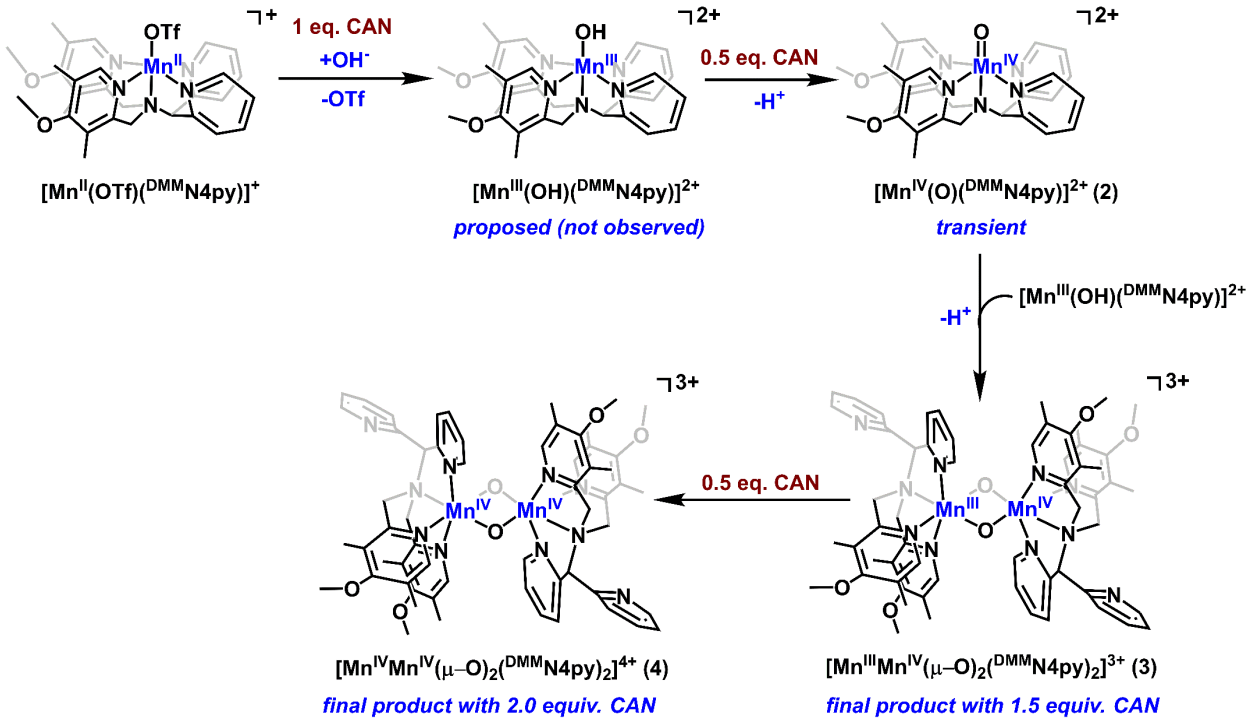

Figure 6. Reaction scheme showing the formation of **2**, **3**, and **4** from the oxidation of $[Mn^{II}(OTf)(^{DMM}N4py)]^{+}$ by CAN.

Spectroscopic Characterization of 4. To evaluate our proposal that **4** contains a bis(μ–oxo)dimanganese(IV,IV) core, we performed EPR and Mn K-edge XAS experiments. The EPR spectrum of $[Mn^{IV}Mn^{IV}(\mu\text{–}O)_2(^{DMM}N4py)_2]^{4+}$ shows a complex signal centered at $g = 2.0$ (Figure S7). The signal resembles an admixture of the EPR spectra of $[Mn^{II}(OTf)(^{DMM}N4py)](OTf)$ and $[Mn^{III}Mn^{IV}(\mu\text{–}O)_2(^{DMM}N4py)_2]^{3+}$ (Figure S6). Spin quantification of the EPR signal indicates that the signal only accounts for ~10% of the Mn in the sample (see Supporting Information). On this basis, we conclude that the majority (~90%) of Mn is in a form that is EPR silent. Several bis(μ-oxo)dimanganese(IV,IV) complexes are EPR silent, which arises from antiferromagnetic coupling between the two Mn^{IV} centers to give an $S = 0$ ground state. Thus, the EPR data are consistent with our formulation of **4** (Figure 6).

Mn *K*-edge XAS near-edge data for **4** show a weak pre-edge feature near 6542 eV and an edge energy of 6551.2 eV (Figure 7). As displayed in Table 1, the edge energy of **4** is slightly higher

than those of **2** (6550.5 eV) and **3** (6550.6).[24, 30] This positive edge shift of **4** relative to **3** is consistent with the higher average Mn oxidation state in **4**. The shift between **4** and **2** might reflect strong covalency within the Mn=O double-bond in **2** that could affect the edge energy.

The pre-edge regions of **2**, **3**, and **4** are remarkably similar (Table 3). The pre-edge peak for **4** could be simulated as three transitions at 6540.5, 6541.6, and 6542.9 eV (Figure S7). These pre-edge energies are nearly identical to those of **2** and **3**, with the exception that a higher-energy transition near 6543 eV was not observed in the bis(μ-oxo)dimanganese(III,IV) complex **3** (Table 1). The analysis of the pre-edge features also reveals that each complex has a similar pre-edge area of ~20, which reflects similar distortions from centrosymmetry for these complexes. Although it might be anticipated that the short Mn=O double-bond in a terminal metal-oxo complex would represent a larger deviation from centrosymmetry than a bis(μ-oxo)dimanganese complex with Mn-O single bonds, the pre-edge area is influenced by several factors, including metal-ligand covalency, metal geometry, and metal oxidation state. A previous study of a bis(μ-oxo)dimanganese(IV,IV) complex supported by derivatives of the salen ligand showed similar pre-edge peak energies (6541.0 and 6542.7 eV), with a larger total area of 36.2 units.

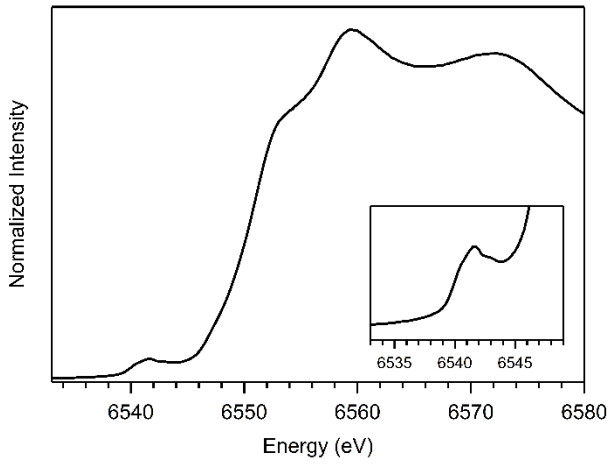

Figure 7. Mn *K*-edge XANES spectrum of $[Mn^{IV}Mn^{IV}(\mu\text{–}O)_2(^{DMM}N4py)_2]^{4+}$ prepared from the reaction of $[Mn^{II}(OTf)(^{DMM}N4py)](OTf)$ and 2 equiv. CAN in 7:3 (v/v) MeCN:H_2O at 0 °C. Inset shows enlarged view of the pre-edge region.

An analysis of the EXAFS data of **4** provides structural information for this complex. The Fourier transform of the EXAFS region of $[Mn^{IV}Mn^{IV}(\mu\text{–}O)_2(^{DMM}N4py)_2]^{4+}$ shows five peaks, including three prominent peaks at *R′* of 1.3, 2.0, and 2.4 Å (Figure 8). The EXAFS data can be well fit using a shell of two O atoms at 1.80 Å, a shell of 3 N atoms at 2.02 Å, a shell of 8 C atoms at 2.88 Å, and a single Mn scatterer at 2.64 Å (Table 2). The goodness of fit and Debye-Waller factors (σ^2) are sensitive to the number of scatterers in each shell, and the best fit is actually achieved with an inner shell of one O atom and two N atoms (Table S1). However, the Debye-Waller factor for the single O-atom shell is unreasonably low (1.98×10^{-3} Å^2). Importantly, the Mn-scatterer distance is not very sensitive to the number of atoms in the shell. In particular, the Mn···Mn and Mn–O separations only vary from their respective values of 2.64 – 2.65 Å and 1.78 – 1.80 Å regardless of the number of scatterers in the O, N, or C shells (Table S1). The average bond distances of Mn–O and Mn–N derived from the best fit for the EXAFS data of $[Mn^{III}Mn^{IV}(\mu\text{-}O)_2(^{DMM}N4py)_2]^{3+}$ are longer than those of $[Mn^{IV}Mn^{IV}(\mu\text{–}O)_2(^{DMM}N4py)_2]^{4+}$ by 0.03 and 0.11 Å, respectively (Table 2, Figure S8).[30] Accordingly, the EXAFS data provide strong support for metric parameters characteristic of a bis(μ-oxo)dimanganese(IV,IV) core.

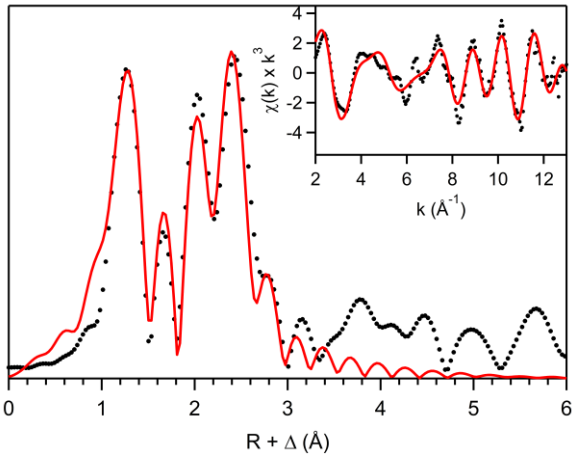

Figure 8. Fourier transform of Mn *K*-edge EXAFS spectrum of $[Mn^{IV}Mn^{IV}(\mu\text{–}O)_2(^{DMM}N4py)_2]^{4+}$ (black dots) and fit (red trace). Inset shows raw *k*-space experimental data (black dots) and the fit (red trace).

Table 2. Metric Parameters from EXAFS Fits results of $[Mn^{IV}Mn^{IV}(\mu\text{-}O)_2(^{DMM}N4py)_2]^{4+}$ (**4**), $[Mn^{III}Mn^{IV}(\mu\text{-}O)_2(^{DMM}N4py)_2]^{3+}$ (**3**), and $[Mn^{IV}(O)(^{DMM}N4py)]^{2+}$ (**2**).[a]

	Mn–O			Mn–N			Mn···Mn			Mn···C	
	n	r (Å)	σ^2 (Å^2)	n	r (Å)	σ^2 (Å^2)	n	r (Å)	σ^2 (Å^2)	n	r (Å)	σ^2 (Å^2)
$[Mn^{IV}Mn^{IV}(\mu\text{–}O)_2(^{DMM}N4py)_2]^{4+}$	2	1.79	7.40	3	2.02	10.5	1	2.64	3.45	6	2.88	6.083
$[Mn^{III}Mn^{IV}(\mu\text{-}O)_2(^{DMM}N4py)_2]^{3+}$	2	1.82	6.0	2	2.05	6.1	1	2.65	3.0	6	2.92	4.2
				2	2.22	2.5						
$[Mn^{IV}(O)(^{DMM}N4py)]^{2+}$	1	1.72	1.26	2	1.94	2.38	-	-	-	3	2.92	2.28
				3	2.10	6.09				3	2.74	8.63

[a] Debye-Waller factors are given in × 10^3. Data for $[Mn^{IV}(O)(^{DMM}N4py)]^{2+}$ and $[Mn^{III}Mn^{IV}(\mu\text{-}O)_2(^{DMM}N4py)_2]^{3+}$ are from ref. 24 and 26, respectively.

DFT Structure of $[Mn^{IV}Mn^{IV}(\mu\text{-}O)_2(^{DMM}N4py)_2]^{4+}$. We used DFT calculations to develop a structure for $[Mn^{IV}Mn^{IV}(\mu\text{–}O)_2(^{DMM}N4py)_2]^{4+}$. On the basis of the EPR data for this complex, we assumed an $S = 0$ ground state. In developing this structure, we considered the X-ray structure of the related $[Mn^{IV}Mn^{III}(\mu\text{–}O)_2(N4py)_2]^{3+}$ complex, which showed that one of the pyridylmethyl groups was not coordinated to a Mn center (Figure 9).[48] In the presence of the bis(μ-oxo)dimanganese core, this κ^4 binding mode for the N4py ligand preserves six coordinate Mn centers. The calculated structure for $[Mn^{IV}Mn^{IV}(\mu\text{–}O)_2(^{DMM}N4py)_2]^{4+}$ shown in Figure 9 is very similar to the X-ray structure of $[Mn^{IV}Mn^{III}(\mu\text{–}O)_2(N4py)_2]^{3+}$. Metric parameters for these structures, as well as those from fits to EXAFS data, are collected in Table 3. The calculated structure for **4** is remarkably consistent with the EXAFS data. The DFT calculated Mn···Mn separation of 2.66 Å is very close to the EXAFS distance (2.64 Å). The DFT structure shows asymmetric Mn–O distances (1.83 and 1.78 Å), and the average given by these distances (1.81 Å) is in good agreement with the O atom EXAFS scatterer at 1.79 Å. Likewise, the average of the Mn–N distances from the DFT structure (2.01 Å) is nearly the same as that from the EXAFS fit (2.02 Å). This high level of agreement lends further credence to our assignment for **4**.

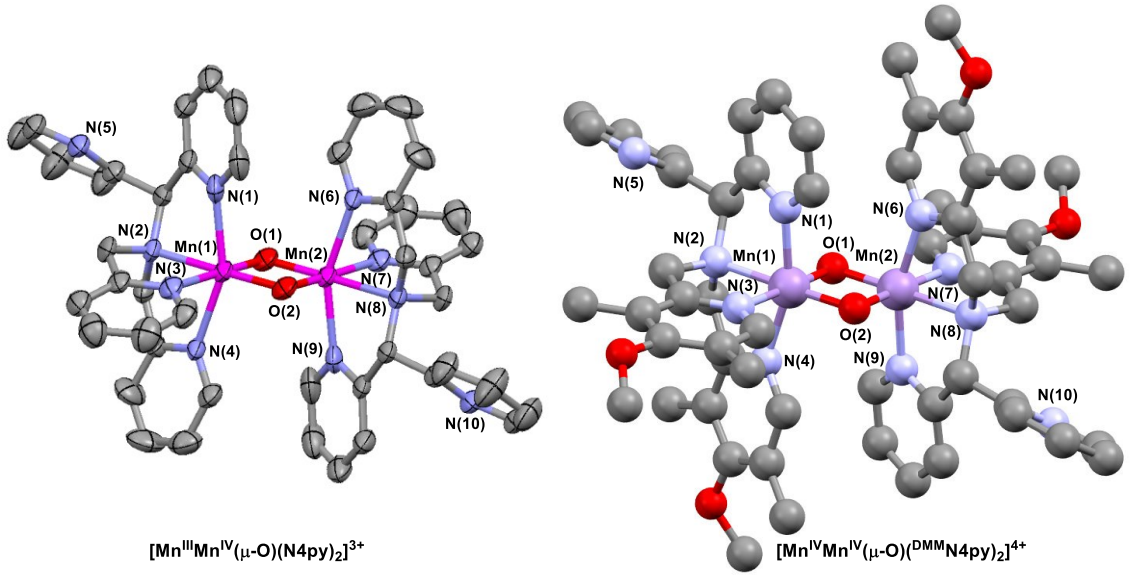

Figure 9. X-ray structure of $[Mn^{III}Mn^{IV}(\mu\text{-}O)_2(N4py)](OTf)_{2.8}(PF_6)_{0.2}$ (left) and DFT structure of $[Mn^{IV}Mn^{IV}(\mu\text{-}O)_2(N4py)]^{4+}$ (right). The X-ray structure is from ref. 50.

Table 3. Selected bond distances (Å) and angles (°) for $[Mn^{IV}Mn^{IV}(\mu\text{-}O)_2(N4py)]^{4+}$ from DFT calculations and EXAFS data analysis and for $[Mn^{III}Mn^{IV}(\mu\text{-}O)_2(N4py)](OTf)_{2.8}(PF_6)_{0.2}$ from X-ray Diffraction (XRD) from EXAFS data analysis.

	$[Mn^{IV}Mn^{IV}(\mu\text{-}O)_2(^{DMM}N4py)]^{4+}$		$[Mn^{III}Mn^{IV}(\mu\text{-}O)_2(N4py)](OTf)_{2.8}(PF_6)_{0.2}$	
	DFT	EXAFS	XRD	EXAFS
Mn(1)···Mn(2)	2.66	2.64	2.6483(8)	2.63
Mn(1) – O(1)	1.83		1.815(3)	
Mn(1) – O(2)	1.78	1.79	1.812(3)	1.79
Mn(2) – O(1)	1.78		1.815(3)	
Mn(2) – O(2)	1.83		1.812(3)	
Mn(1) – N(1)	2.01		2.116(4)	
Mn(1) – N(2)	2.05		2.096(4)	
Mn(1) – N(3)	1.99		2.055(4)	
Mn(1) – N(4)	1.99	2.02	2.143(4)	2.00
Mn(2) – N(6)	1.99		2.143(4)	2.17
Mn(2) – N(7)	1.99		2.055(4)	
Mn(2) – N(8)	2.05		2.096(4)	
Mn(2) – N(9)	2.01		2.116(4)	
O(1)-Mn(1)-O(2)	85.2		86.2(1)	
O(1)-Mn(2)-O(2)	85.2		86.2(1)	
Mn(1)-O(1)-Mn(2)	94.8		93.8(1)	
Mn(1)-O(2)-Mn(2)	94.8		93.8(1)	
N(1)-Mn(1)-N(4)	160.8		155.7(2)	
N(6)-Mn(2)-N(9)	160.8		155.7(2)	

Reactivity of 4 with 2,4-di-tert-butylphenol. We investigated the reactivity of **4** towards 2,4-di-*tert*-butylphenol (2,4-DTBP), as we had previously examined the reactivity of this substrate with **2** and **3**.[30] The addition of 40 equiv. 2,4-DTBP to a 1 mM solution of **4** in MeCN at 25 °C led to the disappearance of the optical signals of **4** (Figure S10), and fits of the decay of the absorption intensity fit a first-order model (k_{obs} = 1.4×10^{-2} s^{-1}). Complex **3** is formed as a product of these reactions in 80% yield, based on the extinction coefficients of **3**. The observation of **3** as a product was unexpected, given that previous studies had demonstrated the ability of **3** to react with 2,4-DTBP.[30] Indeed, the reaction of **3** with 2,4-DTBP gave a k_{obs} of 4.8×10^{-4} s^{-1}, a 29-fold decrease compared to that of **4**.[30] However, the previous experiments for **3** were in CF_3CH_2OH.[30] To evaluate the solvent-dependence of this reaction, we generated **3** in MeCN by oxidation of **1** with 1.5 equiv. CAN and added 40 equiv. 2,4-DTBP at 25 °C. Under these conditions, we observe no reaction of **3** with 2,4-DTBP (Figure S10), indicating a large solvent dependence for this reaction.

Discussion

Although CAN is a powerful oxidant used in stoichiometric and catalytic reactions, it remains difficult to predict which intermediates will be formed by CAN oxidation of a reduced metal complex. In some cases CAN oxidation can yield mononuclear metal(IV)-oxo complexes,[12-16] while in other cases oxo-bridged species transition-metal–cerium adducts are formed.[5, 14, 26-27] In this present work, we sought to better understand the complexities of CAN oxidation by using the $[Mn^{II}(OTf)(^{DMM}N4py)](OTf)$ complex, for which several oxidized intermediates had been previously observed and characterized.[24, 30] The addition of 2 equiv. CAN to $[Mn^{II}(OTf)(^{DMM}N4py)](OTf)$ in a mixture of MeCN and H_2O at room temperature did lead to the formation of the mononuclear Mn^{IV}-oxo complex **2**. However, this species was unstable under

these conditions, only formed in modest yields (~30%), and converted to a new species **4** (Figure 3, top). This result contrasts with that observed for CAN oxidation of several other Mn^{II} complexes, where Mn^{IV}-oxo complexes were generated in high yields.[12-13] Low-temperature reactions of $[Mn^{II}(OTf)(^{DMM}N4py)](OTf)$ with 2.0 equiv. CAN also revealed the initial formation of the Mn^{IV}-oxo complex **2**. In this case, **2** evolved to give the bis(μ-oxo)dimanganese(III,IV) complex **3** before generating **4** (Figure 3, bottom). Both spectroscopic data and chemical reactivity data provide strong support that **4** is a bis(μ-oxo)dimanganese(IV,IV) complex (Figure 6).

When compared with previous reports in the literature, this present study raises several interesting questions. First, why does the Mn^{IV}-oxo complex not form in high yields upon CAN oxidation while **2** can be generated quantitatively by PhIO oxidation? Second, why do we not observed evidence of an oxo-bridged adduct of a Mn complex with cerium?

To address the first question, we propose that both the low yield and stability of the Mn^{IV}-oxo complex **2** in the CAN oxidation reaction relates to the MeCN:H_2O solvent employed. When **2** is generated by PhIO oxidation of $[Mn^{II}(OTf)(^{DMM}N4py)](OTf)$ in TFE, this complex is remarkably stable, having a half-life of 6 hours at 25 °C.[24] We attribute this difference between MeCN:H_2O and TFE to two related factors. First, we have already proposed that the TFE solvent can stabilize the Mn^{IV}-oxo unit through intermolecular hydrogen-bonding interactions.[28] Second, we propose in this work that the bis(μ-oxo)dimanganese(III,IV) complex **3** is generated by the reaction of **2** with a mononuclear Mn^{III}-hydroxo complex (Figure 6). The PhIO oxidation reactions of $[Mn^{II}(OTf)(^{DMM}N4py)](OTf)$ in TFE presumably avoid the formation of any Mn^{III} intermediates, as PhIO is a two-electron oxidant. The ability to form a mononuclear Mn^{IV}-oxo complex in high yields by CAN oxidation thus comes down to a completion between the following reactions: 1) CAN oxidation of the Mn^{III}-hydroxo complex to the Mn^{IV}-oxo complex, and 2) the trapping of the

Mn^{IV}-oxo complex by the Mn^{III}-hydroxo complex to give the bis(μ-oxo)dimanganese(III,IV) complex (Figure 7). We propose that the former reaction must be faster for systems in which CAN oxidation leads to high formation of Mn^{IV}-oxo complexes. In addition, we observe high yields of **2** (30%) when **1** is oxidized using 1.5 equiv. of CAN than when using 2.0 equiv. CAN (15% yield of **2**). We propose that the larger CAN concentration leads to a larger accumulation of the Mn^{III}-hydroxo complex in solution, which more readily traps **2** to give **3**.

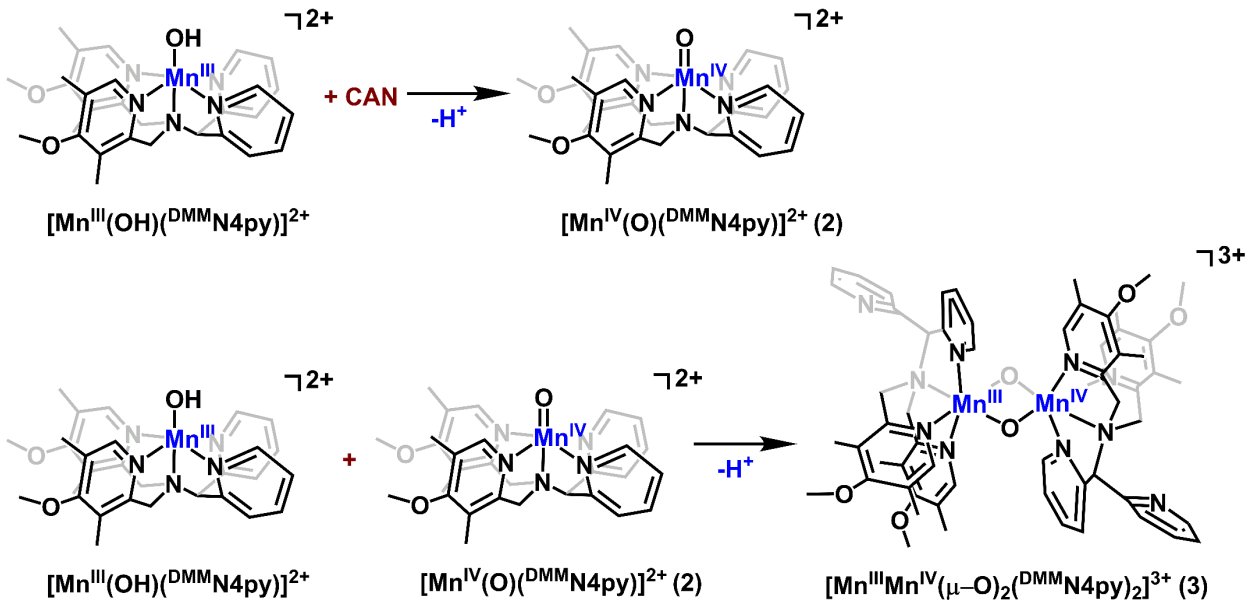

Figure 10. Reactions leading to the formation of the $[Mn^{IV}(O)(^{DMM}N4py)]^{2+}$ (top) and $[Mn^{III}Mn^{IV}(\mu\text{-}O)_2(^{DMM}N4py)_2]^{3+}$ (bottom) complexes.

We now address the second question. Why do we not observe the formation of an oxo-bridged adduct of a Mn complex with cerium? There are growing examples of such intermediates.[14, 27] While we do not have a definitive answer for this question, we offer an observation. In this system, we have convincing evidence that the bis(μ-oxo)dimanganese(III,IV) complex **3** is an intermediate in the CAN oxidation pathway. The geometric structure of **3** would seem to disfavor the formation of a (μ-oxo)manganese-cerium species. For the latter to form, cerium would need to displace one

of the manganese ions, and a spacing filling model of a crystal structure of the analogous $[Mn^{III}Mn^{IV}(\mu\text{-O})(N4py)_2]^{3+}$ complex demonstrates shielding of the oxo ligands (Figure S11), which would prevent attack by cerium. In contrast, the conversion of **3** to **4** by Ce^{IV} oxidation could proceed by an outer-sphere mechanism where steric effects would pose a minimal barrier.

Conclusions

In this work, we have shown that CAN oxidation of a Mn^{II} compound features the formation of several intermediates, including a mononuclear Mn^{IV}-oxo complex, a bis(μ-oxo)dimanganese(III,IV) complex, and a bis(μ-oxo)dimanganese(IV,IV) complex. The final bis(μ-oxo)dimanganese(IV,IV) species was stable and amenable to spectroscopic characterization, while the other intermediates had been previously reported.[24, 30] Future work will explore how reaction conditions can be manipulated to control which intermediates are formed in a predictable fashion.

Supporting Information. EPR and XAS data, EXAFS fits, space-filling diagrams and Cartesian coordinates from DFT computations (PDF).

Acknowledgements. This work was supported by the U.S. National Science Foundation (CHE-2154955 to T. A. J.). The calculations were performed at the University of Kansas Center for Research Computing (CRC), including the BigJay Cluster resource funded through U.S. NSF Grant MRI-2117449. The use of the Stanford Synchrotron Radiation Lightsource, SLAC National Accelerator Laboratory, is supported by the U.S. Department of Energy, Office of Science, Office of Basic Energy Sciences under Contract No. DE-AC02-76SF00515. The SSRL Structural Molecular Biology Program is supported by the DOE Office of Biological and Environmental

Research and by the National Institutes of Health's National Institute of General Medical Sciences (P30GM133894).

References.

1. Piro, N. A.; Robinson, J. R.; Walsh, P. J.; Schelter, E. J., The electrochemical behavior of cerium(III/IV) complexes: Thermodynamics, kinetics and applications in synthesis. *Coord. Chem. Rev.* **2014,** *260*, 21-36.
2. Molander, G. A., Application of lanthanide reagents in organic synthesis. *Chem. Rev.* **1992,** *92* (1), 29-68.
3. Nair, V.; Deepthi, A., Cerium(IV) Ammonium Nitrate-A Versatile Single-Electron Oxidant. *Chem. Rev.* **2007,** *107* (5), 1862-1891.
4. Noyes, A. A.; Garner, C. S., Strong Oxidizing Agents in Nitric Acid Solution. I. Oxidation Potential of Cerous—Ceric Salts. *J. Am. Chem. Soc.* **1936,** *58* (7), 1265-1268.
5. Codolà, Z.; Gómez, L.; Kleespies, S. T.; Que Jr, L.; Costas, M.; Lloret-Fillol, J., Evidence for an oxygen evolving iron–oxo–cerium intermediate in iron-catalysed water oxidation. *Nat. Commun.* **2015,** *6* (1), 5865.
6. Moonshiram, D.; Alperovich, I.; Concepcion, J. J.; Meyer, T. J.; Pushkar, Y., Experimental demonstration of radicaloid character in a Ru^{V}=O intermediate in catalytic water oxidation. *Proc. Nat. Acad. Sci.s* **2013,** *110*, 3765-3770.
7. Fillol, J. L.; Codolà, Z.; Garcia-Bosch, I.; Gómez, L.; Pla, J. J.; Costas, M., Efficient water oxidation catalysts based on readily available iron coordination complexes. *Nat. Chem.* **2011,** *3* (10), 807-813.
8. Ellis, W. C.; McDaniel, N. D.; Bernhard, S.; Collins, T. J., Fast Water Oxidation Using Iron. *J. Am. Chem. Soc.* **2010,** *132* (32), 10990-10991.
9. Grotjahn, D. B.; Brown, D. B.; Martin, J. K.; Marelius, D. C.; Abadjian, M.-C.; Tran, H. N.; Kalyuzhny, G.; Vecchio, K. S.; Specht, Z. G.; Cortes-Llamas, S. A.; Miranda-Soto, V.; van Niekerk, C.; Moore, C. E.; Rheingold, A. L., Evolution of Iridium-Based Molecular Catalysts during Water Oxidation with Ceric Ammonium Nitrate. *J. Am. Chem. Soc.Society* **2011,** *133* (47), 19024-19027.
10. Sridharan, V.; Menéndez, J. C., Cerium(IV) Ammonium Nitrate as a Catalyst in Organic Synthesis. *Chem.l Rev.* **2010,** *110* (6), 3805-3849.
11. McEvoy, J. P.; Brudvig, G. W., Water-Splitting Chemistry of Photosystem II. *Chem. Rev.* **2006,** *106* (11), 4455-4483.
12. Sawant, S.; Wu, X.; Cho, J.; Cho, K.-B.; Kim, S.; Seo, M.; Lee, Y.-M.; Kubo, M.; Ogura, T.; Shaik, S.; Nam, W., Water as an Oxygen Source: Synthesis, Characterization, and Reactivity Studies of a Mononuclear Nonheme Manganese(IV) Oxo Complex. *Angew. Chem. Int. Ed.* **2010,** *122* (44), 8366-8370.
13. Barman, P.; Vardhaman, A. K.; Martin, B.; Wörner, S. J.; Sastri, C. V.; Comba, P., Influence of Ligand Architecture on Oxidation Reactions by High-Valent Nonheme Manganese Oxo Complexes Using Water as a Source of Oxygen. *Angew. Chem. Int. Ed.* **2015,** *127* (7), 2123-2127.
14. Karmalkar, D. G.; Sankaralingam, M.; Seo, M. S.; Ezhov, R.; Lee, Y.-M.; Pushkar, Y. N.; Kim, W.-S.; Fukuzumi, S.; Nam, W., A High-Valent Manganese(IV)–Oxo–Cerium(IV)

Complex and Its Enhanced Oxidizing Reactivity. *Angew. Chem. Int. Ed.* **2019,** *58* (45), 16124-16129.
15. Wu, X.; Yang, X.; Lee, Y.-M.; Nam, W.; Sun, L., A nonheme manganese(IV)-oxo species generated in photocatalytic reaction using water as an oxygen source. *Chem. Commun.* **2015,** *51* (19), 4013-4016.
16. Lee, Y.-M.; Dhuri, S. N.; Sawant, S. C.; Cho, J.; Kubo, M.; Ogura, T.; Fukuzumi, S.; Nam, W., Water as an Oxygen Source in the Generation of Mononuclear Nonheme Iron(IV) Oxo Complexes. *Angew. Chem. Int. Ed.* **2009,** *48* (10), 1803-1806.
17. Parsell, T. H.; Yang, M.-Y.; Borovik, A. S., C−H Bond Cleavage with Reductants: Re-Investigating the Reactivity of Monomeric MnIII/IV−Oxo Complexes and the Role of Oxo Ligand Basicity. *J. Am. Chem. Soc.* **2009,** *131* (8), 2762-2763.
18. Czernuszewicz, R. S.; Su, Y. O.; Stern, M. K.; Macor, K. A.; Kim, D.; Groves, J. T.; Spiro, T. G., Oxomanganese(IV) porphyrins identified by resonance Raman and infrared spectroscopy. Weak bonds and the stability of the half-filled t_{2g} subshell. *J. Am. Chem. Soc.* **1988,** *110* (13), 4158-4165.
19. Makino, R.; Uno, T.; Nishimura, Y.; Iizuka, T.; Tsuboi, M.; Ishimura, Y., Coordination structures and reactivities of compound II in iron and manganese horseradish peroxidases. A resonance Raman study. *J. Biol. Chem.* **1986,** *261* (18), 8376-8382.
20. Groves, J. T.; Stern, M. K., Olefin epoxidation by manganese (IV) porphyrins: evidence for two reaction pathways. *J. Am. Chem. Soc.* **1987,** *109* (12), 3812-3814.
21. Chen, J.; Lee, Y.-M.; Davis, K. M.; Wu, X.; Seo, M. S.; Cho, K.-B.; Yoon, H.; Park, Y. J.; Fukuzumi, S.; Pushkar, Y. N.; Nam, W., A Mononuclear Non-Heme Manganese(IV)–Oxo Complex Binding Redox-Inactive Metal Ions. *J. Am. Chem. Soc.* **2013,** *135*, 6388-6391.
22. Wu, X.; Seo, M. S.; Davis, K. M.; Lee, Y.-M.; Chen, J.; Cho, K.-B.; Pushkar, Y. N.; Nam, W., A Highly Reactive Mononuclear Non-Heme Manganese(IV)–Oxo Complex That Can Activate the Strong C–H Bonds of Alkanes. *J. Am. Chem. Soc.* **2011,** *133* (50), 20088-20091.
23. Leto, D. F.; Ingram, R.; Day, V. W.; Jackson, T. A., Spectroscopic properties and reactivity of a mononuclear oxomanganese(iv) complex. *Chem. Commun.* **2013,** *49* (47), 5378-5380.
24. Massie, A. A.; Denler, M. C.; Cardoso, L. T.; Walker, A. N.; Hossain, M. K.; Day, V. W.; Nordlander, E.; Jackson, T. A., Equatorial Ligand Perturbations Influence the Reactivity of Manganese(IV)-Oxo Complexes. *Angew. Chem. Int. Ed.* **2017,** *56* (15), 4178-4182.
25. Denler, M. C.; Massie, A. A.; Singh, R.; Stewart-Jones, E.; Sinha, A.; Day, V. W.; Nordlander, E.; Jackson, T. A., MnIV-Oxo complex of a bis(benzimidazolyl)-containing N5 ligand reveals different reactivity trends for MnIV-oxo than FeIV-oxo species. *Dalton Trans.* **2019,** *48* (15), 5007-5021.
26. Draksharapu, A.; Rasheed, W.; Klein, J. E. M. N.; Que Jr, L., Facile and Reversible Formation of Iron(III)–Oxo–Cerium(IV) Adducts from Nonheme Oxoiron(IV) Complexes and Cerium(III). *Angew. Chem. Int. Ed.* **2017,** *56* (31), 9091-9095.
27. Gupta, S.; Arora, P.; Kumar, R.; Awasthi, A.; Chandra, B.; Eerlapally, R.; Xiong, J.; Guo, Y.; Que Jr, L.; Draksharapu, A., Formation of a Reactive [Mn(III)−O−Ce(IV)] Species and its Facile Equilibrium with Related Mn(IV)(OX) (X = Sc or H) Complexes. *Angew. Chem. Int. Ed.* **2024,** *63* (3), e202316378.
28. Massie, A. A.; Denler, M. C.; Singh, R.; Sinha, A.; Nordlander, E.; Jackson, T. A., Structural Characterization of a Series of N5-Ligated MnIV-Oxo Species. *Chem. Eur. J.* **2020,** *26* (4), 900-912.

29. Singh, P.; Denler, M. C.; Mayfield, J. R.; Jackson, T. A., Differences in chemoselectivity in olefin oxidation by a series of non-porphyrin manganese(iv)-oxo complexes. *Dalton Trans.* **2022,** *51* (15), 5938-5949.
30. Lee, Y.; Jackson, T. A., Ligand Influence on Structural Properties and Reactivity of Bis(μ-oxo)dimanganese(III,IV) Species and Comparison of Reactivity with Terminal Mn^{IV}-oxo Complexes. *ChemistrySelect* **2018,** *3* (47), 13507-13516.
31. Rana, S.; Dey, A.; Maiti, D., Mechanistic elucidation of C–H oxidation by electron rich non-heme iron(iv)–oxo at room temperature. *Chem. Commun.* **2015,** *51* (77), 14469-14472.
32. Dixon, N. E.; Lawrance, G. A.; Lay, P. A.; Sargeson, A. M.; Taube, H., Trifluoromethanesulfonates and Trifluoromethanesulfonato-O Complexes. *Inorg. Synth.* **1990**, 70-76.
33. Ravel, B.; Newville, M., ATHENA, ARTEMIS, HEPHAESTUS: data analysis for X-ray absorption spectroscopy using IFEFFIT. *J. Synchrotron Radiat.* **2005,** *12* (4), 537-541.
34. Rehr, J. J.; Mustre De Leon, J.; Zabinsky, S. I.; Albers, R. C., Theoretical x-ray absorption fine structure standards. *J. Am. Chem. Soc.* **1991,** *113* (14), 5135-5140.
35. Wojdyr, M., Fityk: a general-purpose peak fitting program. *J. Appl. Crystallogr.* **2010,** *43* (5 Part 1), 1126-1128.
36. Neese, F. *ORCA - an ab initio, Density Functional and Semiempirical Program Package*, 2.9.1; Max Planck Institut für Chemische Energiekonversion: Mülheim an der Ruhr, Germany, 2013.
37. Neese, F., Software update: The ORCA program system—Version 5.0. *Wiley Interdiscip. Rev. Comput. Mol. Sci.* **2022,** *12* (5), e1606.
38. Becke, A. D., Density-functional Thermochemistry. III. The Role of Exact Exchange. *J. Chem. Phys.* **1993,** *98* (7), 5648-5652.
39. Lee, C.; Yang, W.; Parr, R. G., Development of the Colle-Salvetti Correlation-energy Formula into a Functional of the Electron Density. *Phys. Rev. B* **1988,** *37* (2), 785-789.
40. Grimme, S.; Antony, J.; Ehrlich, S.; Krieg, H., A consistent and accurate ab initio parametrization of density functional dispersion correction (DFT-D) for the 94 elements H-Pu. *J. Chem. Phys.* **2010,** *132* (15), 154104.
41. Grimme, S.; Ehrlich, S.; Goerigk, L., Effect of the damping function in dispersion corrected density functional theory. *J. Comput. Chem.* **2011,** *32* (7), 1456-1465.
42. Schäfer, A.; Horn, H.; Ahlrichs, R., Fully optimized contracted Gaussian basis sets for atoms Li to Kr. *J. Chem. Phys.* **1992,** *97* (4), 2571-2577.
43. Schäfer, A.; Huber, C.; Ahlrichs, R., Fully Optimized Contracted Gaussian Basis Sets of Triple Zeta Valence Quality for Atoms Li to Kr. *J. Chem. Phys.* **1994,** *100*, 5829-5835.
44. Marenich, A. V.; Cramer, C. J.; Truhlar, D. G., Universal Solvation Model Based on Solute Electron Density and on a Continuum Model of the Solvent Defined by the Bulk Dielectric Constant and Atomic Surface Tensions. *J. Phys. Chem. B* **2009,** *113* (18), 6378-6396.
45. C. Lee, W. Yang, R. G. Parr, *Phys. Rev. B* **1988**, *37*, 785-789.
46. A. V. Marenich, C. J. Cramer, D. G. Truhlar, *J. Phys. Chem. B* **2009**, *113*, 6378-6396.
47. Cooper, S. R.; Dismukes, G. C.; Klein, M. P.; Calvin, M., Mixed valence interactions in di-μ-oxo bridged manganese complexes. Electron paramagnetic resonance and magnetic susceptibility studies. *J. Am. Chem. Soc.* **1978,** *100* (23), 7248-7252.
48. Goodson, P. A.; Glerup, J.; Hodgson, D. J.; Michelsen, K.; Weihe, H., Syntheses and characterization of binuclear manganese(III,IV) and -(IV,IV) complexes with ligands related to N,N'-bis(2-pyridylmethyl)-1,2-ethanediamine. *Inorg. Chem.* **1991,** *30* (26), 4909-4914.

49. Krewald, V.; Lassalle-Kaiser, B.; Boron, T. T., III; Pollock, C. J.; Kern, J.; Beckwith, M. A.; Yachandra, V. K.; Pecoraro, V. L.; Yano, J.; Neese, F.; DeBeer, S., The Protonation States of Oxo-Bridged MnIV Dimers Resolved by Experimental and Computational Mn K Pre-Edge X-ray Absorption Spectroscopy. *Inorg. Chem.* **2013,** *52* (22), 12904-12914.
50. Leto, D. F.; Chattopadhyay, S.; Day, V. W.; Jackson, T. A., Reaction landscape of a pentadentate N5-ligated MnII complex with O2- and H2O2 includes conversion of a peroxomanganese(iii) adduct to a bis(μ-oxo)dimanganese(iii,iv) species. *Dalton Trans.* **2013,** *42* (36), 13014-13025.

Table of Contents Graphic

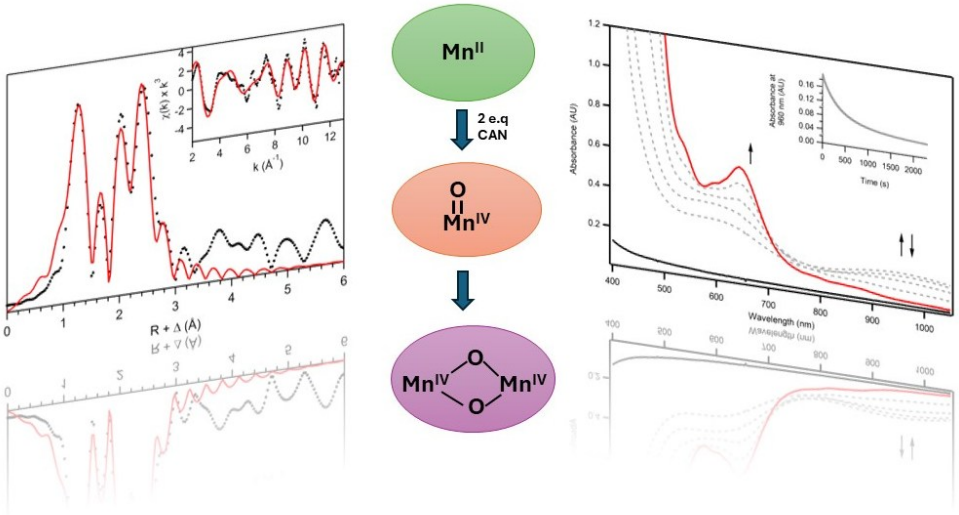

Synopsis

The oxidation of a Mn^{II} complex with ceric ammonium nitrate leads to the sequential formation of Mn^{IV}-oxo, bis(μ-oxo)dimanganese(III,IV), and bis(μ-oxo)dimanganese(IV,IV) intermediates, revealing a rich reaction landscape.